AIAA SciTech Forum
23-27 January 2023, National Harbor, MD & Online
AIAA SCITECH 2023 Forum

10.2514/6.2023-1419

Surrogate Modeling of Orbital Decay of Lunar Orbits

Maxime Varoqui*, Michael J. Steffens †, and Dimitri N. Mavris ‡
Aerospace Systems Design Laboratory, Georgia Institute of Technology, Atlanta, GA, 30332

Operations in cislunar space are expected to greatly increase over the next decade, which will place a heightened demand on satellites operating in cislunar space. The orbit selection of the satellites is a key parameter of the mission. Orbital decay can present significant challenges for some lunar orbits due to gravitational perturbations. This study focuses on developing a fast method to assess the decay of lunar orbits. The method is based on modeling lunar orbits propagation in the presence of these perturbations to quantify orbital decay as a function of orbital parameters, then using the model to generate data and fit surrogate models. Results from this effort will enable decision makers to trade performance and station-keeping costs associated with relevant lunar orbits.

I. Nomenclature

a (SMA)	=	Semi-major axis
e (ECC)	=	Eccentricity
i $(INCL)$	=	Inclination
Ω $(RAAN)$	=	Right Ascension of the Ascending Node
ω (AOP)	=	Argument of Perigee
M	=	Mean Anomaly
DoE	=	Design of Experiments
PNT	=	Positioning, Navigation and Timing

II. Introduction

Satellite activity around the Moon is expected to increase in the coming decades. Proposed activities include scientific studies, human presence, PNT or other architectures, and even tourism [1][2]. One of the challenges of operating in cislunar space is the significant gravitational perturbations that can make lunar orbits very unstable. From a design perspective, this instability complicates orbit selection, and sometimes requires spacecraft to perform station keeping (SK) maneuvers. Significant research for long term lunar orbits have focused on lunar frozen orbits, where the various gravitational perturbations are minimized and the orbits are relatively stable [3, 4]. The goal of this study is to understand and quantify the orbital instability of lunar orbits with respect to the relevant orbital parameters. Such a capability would allow architects of satellite constellations to quickly trade performance benefits of lunar orbits against costs (station keeping or limited mission duration) of operating in those orbits.

III. Background and Problem Definition

While Apollo missions' main purpose was to send a human to the Moon, new space missions have now higher expectations regarding lunar operations. The Artemis [5] mission that is to launch in 2024, has two objectives: first, to achieve human landing by 2024 with reduced risks, and second, to prepare the ground for future space exploration missions. The Moon is to become a strategic passage point for space exploration. Missions like Artemis or the Gateway mission [6] confirm the importance of Earth's satellite either as a host for permanent lunar sites or for outposts orbiting in its sphere of influence. In order to empower potential scientists or autonomous equipment either on the ground or in orbit with PNT and communication services, new lunar infrastructures are needed. LunaNet, for example, aspires to

*Graduate Research Assistant, Aerospace Systems Design Laboratory, School of Aerospace Engineering
†Research Engineer II, Aerospace Systems Design Laboratory, School of Aerospace Engineering, AIAA member.
‡S.P. Langley Distinguished Regents Professor and ASDL Director, Aerospace Systems Design Laboratory, School of Aerospace Engineering, AIAA Fellow.

develop a terrestrial-like internet for lunar users based on a wide network communicating with Earth and lunar ground sites as well as on lunar orbiters [7]. The main issue of lunar orbiters is their decay. Because of perturbations, they are driven to slowly deviate from their original orbits. The main perturbations a spacecraft is subjected to are its drag, the solar radiation pressure, the non-spherical shape of the body it is orbiting around, and the presence of other heavy bodies in its vicinity [4]. An accurate model is required for each one of these perturbations in order to be able to correctly predict a spacecraft orbit and avoid critical deviations of trajectories. Thanks to the Gravity Recovery and Interior Laboratory (GRAIL) [8] mission launched in 2011 by NASA, scientists now possess a very accurate gravity model of the Moon that helps evaluate the magnitude of this perturbation.

Orbital perturbations can be addressed through station keeping maneuvers, effectively altering the velocity vector of satellites to maintain desired orbits. These maneuvers require propellant to be performed and are thus to be optimized to maximize the lifespan of the spacecraft. Often, station keeping maneuvers can be minimized by selecting orbits that are least influenced by the gravitational perturbations. Therefore, it is useful to understand the instability of specific lunar orbits during mission planning and constellation design.

The goal of this study is to develop and implement an approach to quickly evaluate the decay of lunar orbits. The tool is envisioned for use to facilitate the selection of the initial insertion orbits of a constellation of satellites to meet the mission objectives of future cislunar operations.

IV. Technical approach

This effort aims at providing an effective way to quantify orbit cost in orbit/constellation design. This orbit cost could be addressed by either providing station keeping efforts, or allowing the orbit to degrade and limiting the lifetime of the orbit. Traditionally, only frozen orbits have been considered. However, this restriction drastically limits the amount of orbital space that is available and could heavily affect the performance of the overall design. One approach to understand the orbital decay is to numerically propagate the orbits of interest. This method is computationally expensive, especially for a broad design space where a lot of alternatives are studied, and would slow down the design process. Surrogate modeling provides an effective way to support the orbit/constellation design process without incurring as much computational cost. The surrogate models will be based on data from lunar orbits propagated by the tool. The following sections describe the lunar orbital environment, propagation model, and surrogate modeling approach.

The first step in addressing these objectives is to understand and perform the propagation of lunar orbits. For this effort, the long term variations in the orbital parameters are of specific interest. Frozen orbits are a subset of lunar orbits where the long term variations are minimized, and in theory set to 0, and are therefore considered stable [9]. This study includes but is not limited to frozen orbits.

A. Lunar Orbital Forces

Spacecraft in orbit are subject to a number of forces, including gravity, drag and solar radiation pressure. For lunar orbits, given the absence of atmosphere, drag is not considered. Moreover, in the scope of this study solar radiation pressure can be neglected [4]. It should be noted that the method presented here is not predicated on those assumptions. A traditional Keplerian orbit assumes a single uniform gravity source. A spacecraft orbiting the Moon, however, experiences a non-uniform gravity field [10] and perturbations due third-body effects of the Earth and other bodies.

The non-uniform gravity field generated by the Moon arises from the oblateness effect of the Moon and the presence of mascons [11]. Mascons are mass concentrations on the Moon, which result in density changes throughout the Moon and add up to the non-uniformity of the gravity field. The gravity field can be modeled using spherical harmonic functions, which can be defined to higher orders depending on data available and accuracy needed. Until the GRAIL [8] mission, the Moon gravity model was not very accurate. But thanks to the data gathered by its two modules that communicated together to detect any small deviation in relative distance between them, the mission enabled the creation of an improved gravity field, which is now the most accurate model that any space body possesses. While on Earth, the most dominant perturbing term is the oblateness term J_2 (more than 1000 times as large as any other gravity model coefficient [12]), it is not the case for the Moon. The lunar gravity coefficients J_2 and C_{22} are the same order of magnitude. According to previous studies, J_2 and C_{22} are the most significant terms of the lunar gravity field function. Thus, the perturbation potential leveraged in this study will feature the gravity model of the Moon until the C_{22} term, while higher order terms will be neglected [13].

The relevant third-body effects for lunar orbit include the Earth and sun. For this effort, only Earth effects will be included, as effects from the sun are much smaller [4]. Additionally, it is assumed that the Moon describes a circular orbit around the sun [14].

These assumptions lead us to the following expressions of the perturbing gravitational potential truncated at the 2^{nd} degree for the third-body effects [3], and with a maximum precision of 10^{-4}[14]:

$$R_p = -\frac{J_2 \mu R_M^2}{r^3} * (1.5 * sin(i)^2 * sin^2(f+\omega) - 0.5) + \frac{kn_3^2 r^2}{2} \left[3[cos(f+\omega) * cos(h) - sin(f+\omega) sin(h) cos(i)]^2 - 1\right] + \frac{3C_{22}\mu R_M^2}{r^3} sin(i)^2 s(f+\omega)^2 - 1 + 2[cos(h)cos(f+\omega) - sin(h)cos(i)sin(f+\omega)^2]$$

where $h = \Omega - n_3 t$; $k = \frac{m_E}{m_E + m_M}$; i, Ω, ω, f are the classical orbital elements; n_3 is the angular velocity of the Moon around the Earth; and m_E, m_M are the mass of the Earth and the Moon respectively.

It is useful in this context to only consider the long-term perturbations to the orbit. Shorter and medium term perturbations will have less of an effect on the long-term stability of the orbits [3]. The equations of motion for the long-term perturbations can be developed for the classical orbital elements, and are shown below [4].

$$\begin{aligned}
\dot{\bar{a}} &= 0 \\
\dot{\bar{e}} &= \frac{15kn_3^2\bar{a}^{3/2}}{8\sqrt{\mu}} \bar{e}\sqrt{1-\bar{e}^2} \sin^2\bar{i} \sin 2\bar{\omega} \\
\dot{\bar{i}} &= -\frac{15kn_3^2\bar{a}^{3/2}}{16\sqrt{\mu}} \frac{\bar{e}^2}{\sqrt{1-\bar{e}^2}} \sin 2\bar{i} \sin 2\bar{\omega} \\
\dot{\bar{\Omega}} &= -\frac{3J_2\sqrt{\mu}R_M^2}{2\bar{a}^{7/2}\left(1-\bar{e}^2\right)^2} \cos\bar{i} + \frac{3kn_3^2\bar{a}^{3/2}}{8\sqrt{\mu}\sqrt{1-\bar{e}^2}} \left(5\bar{e}^2\cos 2\bar{\omega} - 3\bar{e}^2 - 2\right)\cos\bar{i} \\
\dot{\bar{\omega}} &= \frac{3J_2\sqrt{\mu}R_M^2}{4\bar{a}^{7/2}\left(1-\bar{e}^2\right)^2} \left(5\cos^2\bar{i} - 1\right) + \frac{3kn_3^2\bar{a}^{3/2}}{8\sqrt{\mu}\sqrt{1-\bar{e}^2}} \left[\left(5\cos^2\bar{i} - 1 + \bar{e}^2\right) + 5\left(1 - \bar{e}^2 - cos^2\bar{i}\right)\cos 2\bar{\omega}\right] \\
\dot{\bar{M}} &= \frac{\sqrt{\mu}}{\bar{a}^{3/2}} + \frac{3J_2\sqrt{\mu}R_M^2}{4\bar{a}^{7/2}\left(1-\bar{e}^2\right)^{3/2}} \left(3\cos^2\bar{i} - 1\right) - \frac{kn_3^2\bar{a}^{3/2}}{8\sqrt{\mu}} \left[\left(3\bar{e}^2 + 7\right)\left(3\cos^2\bar{i} - 1\right) + 15\left(1 + \bar{e}^2\right)\sin^2\bar{i}\cos 2\bar{\omega}\right]
\end{aligned} \tag{1}$$

where $\{\ \bar{a}, \bar{e}, \bar{i}, \bar{\Omega}, \bar{\omega}, \bar{M}\ \}$ are the averaged classical orbital elements, semimajor axis, eccentricity, inclination, right ascension of ascending node, argument of perigee, and mean anomaly.

B. Orbit Propagation

The differential equations in Equation 1 can be numerically propagated to simulate lunar orbits based on input orbital parameters. For this effort, a fixed time step Runge-Kutta method was used to integrate the equations of motion. Each orbit was defined using the orbital elements in Section IV.A. Mean anomaly M was initialized at 0 in each case.

C. Measuring Orbit Deviations

In most lunar orbits, the orbital parameters will change through time. The rate of orbital changes themselves are also a function of the orbital parameters, as seen in Equation 1. For this effort, a metric was needed to quantify how much an orbit would changes as a function of the orbital parameters. Two options considered were to quantify the change in orbital elements over a single period of time for all orbits considered, or to quantify the change over a single orbit. In this case, the changes in orbital elements were compared based on the period of the orbit.

$$\begin{aligned}
\Delta a &= a_{initial} - a_{final} \\
\Delta e &= e_{initial} - e_{final} \\
\Delta i &= i_{initial} - i_{final} \\
\Delta\Omega &= \Omega_{initial} - \Omega_{final} \\
\Delta\omega &= \omega_{initial} - \omega_{final}
\end{aligned} \tag{2}$$

The final value for mean anomaly M was always 2π, as this represents a completed orbit.

D. Orbit Station Keeping

Spacecraft operating in unstable orbits plan station keeping maneuvers to maintain the desired orbit throughout the lifetime of the spacecraft. These station keeping maneuvers can be quantified by the ΔV associated with each maneuver. Each maneuver is based on the current and desired state, as well as the time of transfer. There are many maneuvers available between orbits based on different times of flight. Maneuvers between unstable orbits are complicated by the fact that the transfer orbit is itself unstable.

Lambert's problem is a method that allows to establish the transfer orbit between two points A and B in space (with initial and final velocities) depending on specific time of flight [12] (see Figure 1). With the transfer orbit known alongside with the position vectors of the current (r_1) and target (r_2) orbits, the velocity vectors at A (v_1) and B (v_2) on the transfer orbit can be derived. These two vectors are respectively subtracted to the velocity vectors at A and B on the initial orbit propagated. This leads to the values of ΔV at A and B that respectively enable the transition form the current orbit to the transfer orbit and then from the transfer orbit to the target orbit which is in the case of station keeping, the initial orbit of the spacecraft. Finally, by adding up the two ΔV, the total required velocity change for the SK maneuver is derived.

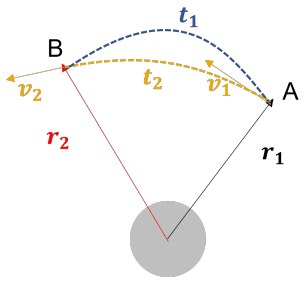

Fig. 1 Illustration of Lambert's problem

For this effort, the metrics in Section IV.C are used to quantify the cost of operating in a specified orbit. Future work will include research on optimal maneuvers to minimize orbital decay as well as ΔV requirements, while taking specific thrust performance into consideration. These considerations can include how often to perform the station keeping maneuvers.

E. Surrogate Models and Design of Experiments

As previously mentioned, the tool is developed to assess the orbital decay of satellites orbiting around the Moon. Because of forces balancing each other out, some orbits are more stable than others and present a reduced orbital decay. These orbits are called frozen orbits and are interesting in a sense that they minimize ΔV for station keeping. The orbital elements yielding such orbits can be obtained analytically [3], with some assumptions regarding the perturbations. However, there may be cases where performance achieved from a certain orbit may be worth the station keeping costs incurred. It is therefore desirable to consider a much wider range of lunar orbits. Propagating each of these orbits would represent a significant computational cost. The fields of Design of Experiments (DoE) and surrogate modeling enable the creation of analytical models representing underlying data, in this case data pertaining to the stability of lunar orbits. This would allow the user to virtually instantaneously compute the orbital error based on the input of any set of orbital elements. The design space of interest is represented by continuous orbital parameters. A DoE intelligently samples the design space to get a sufficiently high density of the design space. It selects the different points the user needs to run (sets of orbital elements $a, e, i, \Omega, \omega, M$) [3]. Thanks to this sampling, the user can run a limited number of cases that, in the whole, reflect the global trend and logic of the design space. Surrogate models then act as bridges between these design points, as they are the interpolating functions linking inputs (orbital elements) to outputs (orbital decay). The design variables as well as their ranges used for the DoE are shown in Table 1. The initial value for mean anomaly M was always zero.

The DoE was a Latin hypercube (LHC) to fill the gap between the boundary points thanks to an optimal spacing algorithm [15]. For this study, nested LHC designs were used. Nested LHCs allow for varying the number of cases used in surrogate model fitting while reusing some of the cases and maintaining the LHC design [16].

Table 1 Design of Experiment variables and ranges

Notation	Definition	Range	Unit
a	Semi-major axis	$1758 - 20,000$	km
e	Eccentricity	$0 - 0.98$	/
i	Inclination	$0 - 180$	degree
Ω	Right Ascension of the Ascending Node	$0 - 360$	degree
ω	Argument of Perigee	$0 - 360$	degree

V. Results

The following sections present the results for this effort starting with the orbit perturbations for a single lunar orbit, then showing the results from the DoE and surrogate model fitting, finally discussing frozen orbits and simplified ΔV calculations.

A. Results for Single Orbit

Each lunar orbit is initialized by defining the classical orbital elements $\{a, e, i, \Omega, \omega, M\}$. An example orbit is defined in Table 2.

Table 2 Orbital elements for single lunar orbit

Orbital Element	Value	Unit
a	7758	km
e	0.4	/
i	50	degree
Ω	0	degree
ω	100	degree
M	0	degree

The period of an orbit is calculate as $T = 2\pi\sqrt{a^3/\mu}$ for each orbit. For this example, the orbital period is just under 17 hr, 1 min, and 56 sec. Figure 2 below shows the orbit.

Table 3 shows the changes in orbital elements for this orbit over the course of a single orbital period. The change in semi major axis a is zero, as the equations of motion (Equation 1) show that the rate of change $\dot{a}$ is defined as 0. The change in mean anomaly M is 2π, indicating a single orbital period as expected. The other changes in eccentricity, inclination, right ascension of ascending node, and argument of perigee represent the effect of gravitational perturbations and third-body effects on the orbit. These deviations would grow non-linearly over time. Figure 3 shows the orbital trajectory over 100 periods. Figure 4 shows the non-linear changes in orbital parameters over time.

Table 3 Changes in orbital elements for example orbit

Orbital Element	ΔValue	Unit
a	0	km
e	$5.76E-04$	/
i	$-2.301E-04$	rad
Ω	$3.65E-03$	rad
ω	$1.27E-03$	rad
M	6.28	rad

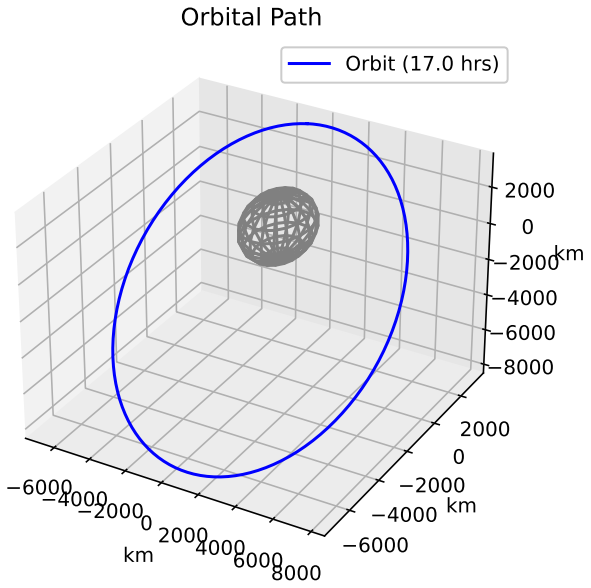

Fig. 2 Example orbit trajectory

B. Design of Experiment Results

The DoE defines a set of lunar orbits that covers the design space of interest, shown in Table 1. The experimental design is a nested LHC design. For a nested LHC, an initial number of cases and layers is selected; the design used in this study had 25 initial cases and 11 layers. The nested design results in an LHC design for each layer up to the number of layers. Each LHC design has $25 \times 2^{(n-1)}$ cases, where n is the layer number starting from 1. The first set of cases has 25 cases, and the second set then has 50 cases, where the first 25 cases of the second set are equivalent to the cases in the first set. This pattern continues to the highest layer selected, in this case 11, resulting in 25, 600 total cases. This setup means that if more cases are needed, the next set of cases could be selected by adding a layer (layer 12) while still using all the cases from the previous layer. Table 4 illustrates the experimental design. The value for mean anomaly M is always initialized at zero.

Table 4 Subset of experiment design

Case Number	a	e	i	Ω	ω	M
1	11,178	0.99345	13.376	204.57	105.71	0
2	8,151.9	0.72118	157.68	264.9	198.49	0
3	2,679.5	0.6042	17.169	101.56	119.13	0
...						
25,599	8,262.8	0.86104	6.3582	247.73	50.234	0
25,600	7,488.6	0.25123	72.135	313.66	127.29	0

Not all the cases in the DoE were physically realisable, as some orbits intercepted (crashed into) the Moon. For each case, if $a(1-e) \leq R_{Moon}$, the case was ignored. In this experimental design, about 23% of the cases represented physically impossible orbits, and were therefore ignored. Figure 5 shows a scatter-plot of the orbital changes for a single orbit for each of the cases ran. It is interesting to note some of the patterns that emerge from this analysis.

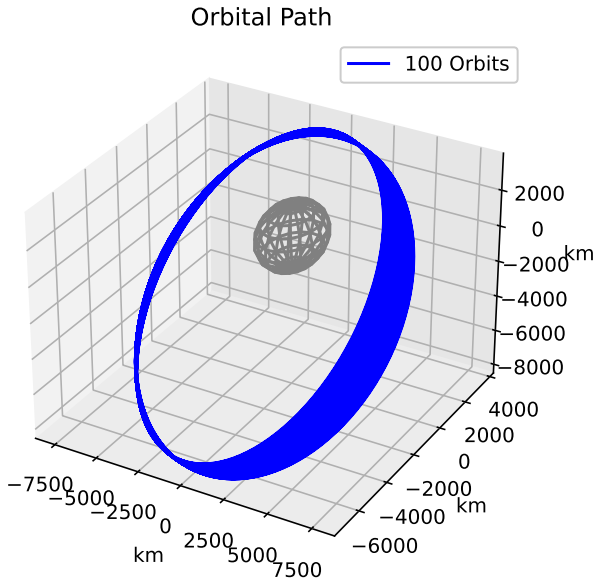

Fig. 3 Orbit trajectory over 100 periods

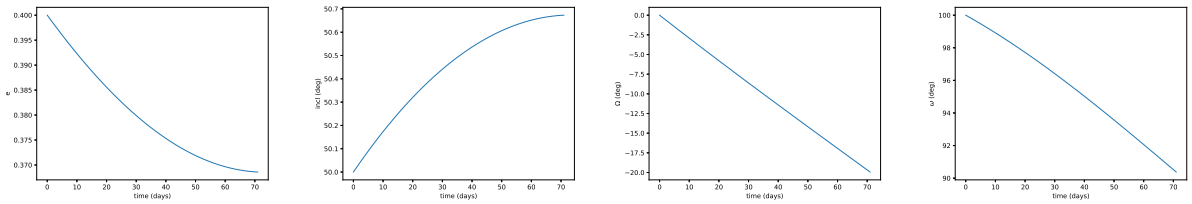

(a) Eccentricity variation **(b) Inclination variation** **(c) Right ascension of ascending node variation** **(d) Argument of perigee variation**

Fig. 4 Orbital parameter variations over 100 orbits

C. Surrogate Models

The data from the DoE can be used to fit surrogate models. In this case, neural networks were used as the approximating function [17]. The neural networks were designed with 2 layers, and activation functions included hyperbolic tangent, linear, and Gaussian; however, many other activation functions are available [18]. The statistical analysis tool JMP was used to train the models [19]. The training was conducted using k-fold cross-validation, which relies on splitting the date into k segments, and alternating which are used for training vs validation [20]. When fitting surrogate models to the smaller LHC DoE's, the goodness of fits were also validated using the remaining data available. Models were compared visually using the actual by predicted and residual by predicted plots, as well as by considering the R^2 and $RMSE$ values for both training and validation data sets.

The smallest LHC design used to fit data consisted of 3200 total cases, of which 2440, or 76.25%, were physically realisable orbits. Table 5 shows the neural network architectures for each of the outputs. Figure 6 shows the goodness of fit plots and Table 6 shows the R^2 and $RMSE$ values for the training and validation data sets. While a good fit was achieved using the k-fold validation method, it performs fairly poorly when the remaining available data is considered.

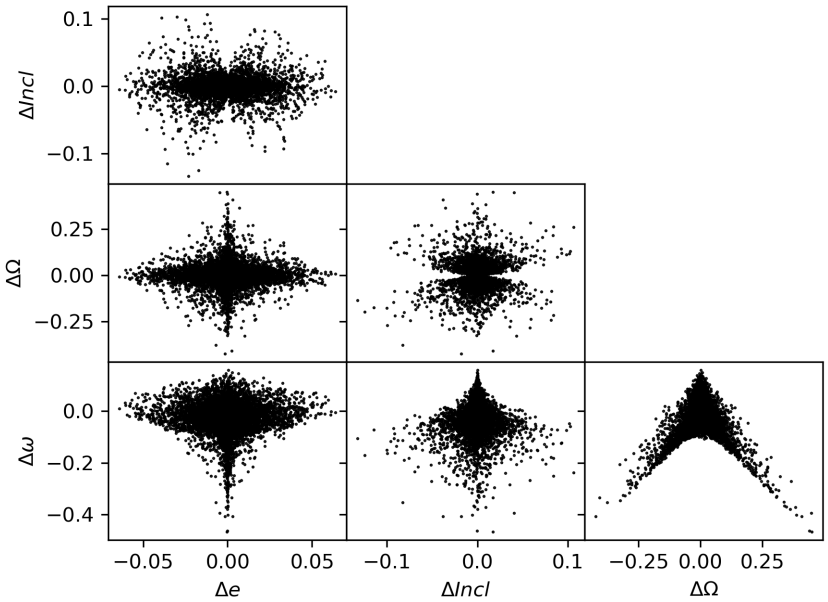

Fig. 5 Scatter-plot of DoE results

Table 5 Neural network architectures for 3200 **case design**

Output	First Layer			Second Layer		
	TanH	Linear	Gaussian	TanH	Linear	Gaussian
Δe	7	7	7	7	7	7
$\Delta Incl$	8	8	8	8	8	8
$\Delta\Omega$	7	7	7	7	7	7
$\Delta\omega$	7	7	7	7	7	7

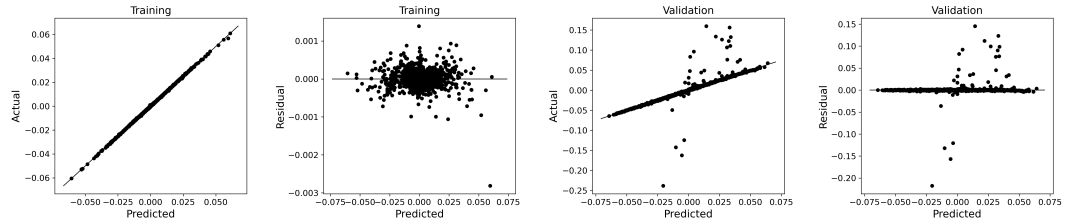

(a) Δe

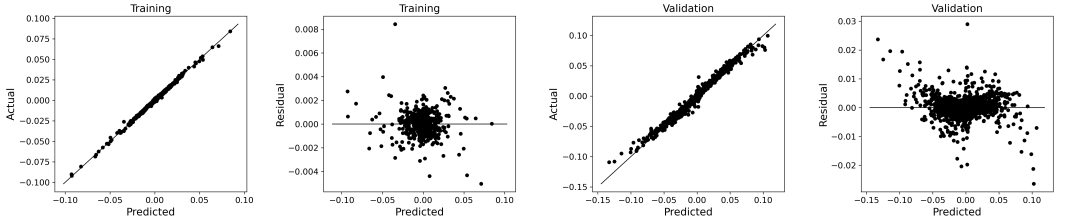

(b) $\Delta Incl$

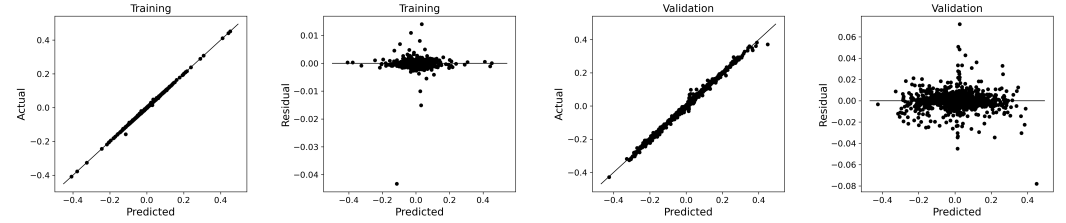

(c) $\Delta\Omega$

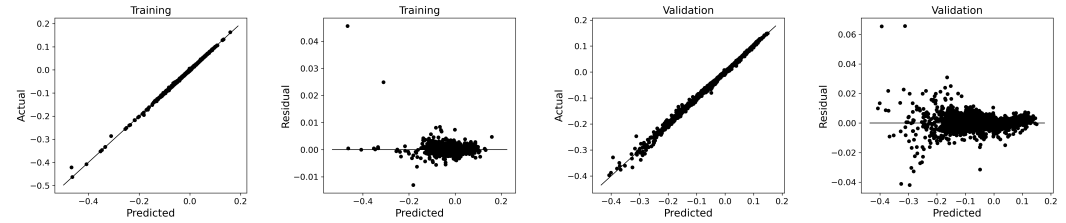

(d) $\Delta\omega$

Fig. 6 Actual and residual by predicted for training and validation for 3200 **case design**

Table 6 Goodness of fit metrics for training with 3200 **case design**

	Δe		$\Delta Incl$		$\Delta\Omega$		$\Delta\omega$	
	Training	Validation	Training	Validation	Training	Validation	Training	Validation
R^2	0.9996	0.8760	0.9956	0.9844	0.9991	0.9968	0.9988	0.9976
$RMSE$	0.0001810	0.003589	0.0005667	0.001132	0.001230	0.002220	0.001535	0.002029

The next LHC design considered used 6400 cases, of which 4789, or 74.83%, were physically realisable orbits. Table 7 shows the neural network architectures for each of the outputs. Figure 7 shows the goodness of fit plots and Table 8 shows the R^2 and $RMSE$ values for the training and validation data sets. The plots and goodness of fit metrics indicate a better estimate of the output metrics than the 3200 case design. Specifically, the R^2 values are all 0.99 or higher for both training and validation, and visual inspection of the validation actual by predicted plots in Figure 7 (third

plot in each row) indicate a consistent accurate estimate. This is expected, as more data was provided to the model.

Table 7 Neural network architectures for 6400 case design

Output	First Layer			Second Layer		
	TanH	Linear	Gaussian	TanH	Linear	Gaussian
Δe	6	6	6	6	6	6
$\Delta Incl$	6	6	6	6	6	6
$\Delta\Omega$	6	6	6	6	6	6
$\Delta\omega$	8	8	8	8	8	8

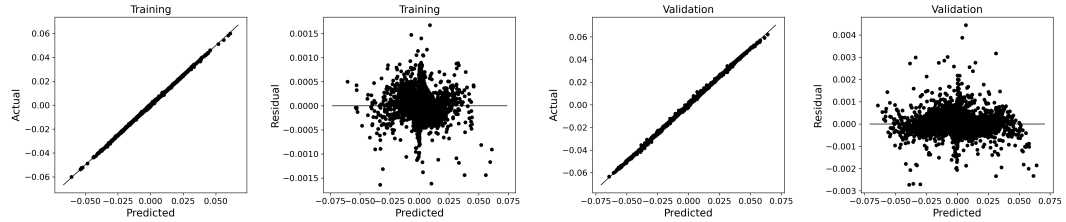

(a) Δe

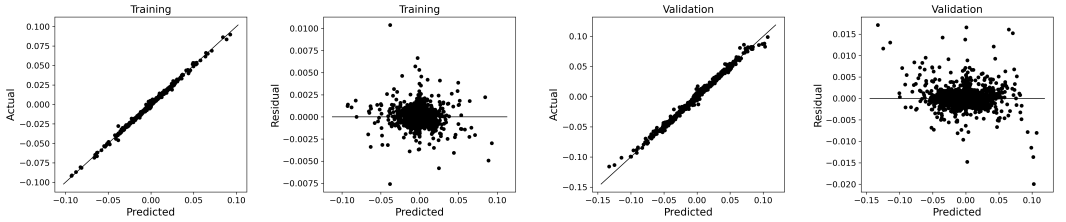

(b) $\Delta Incl$

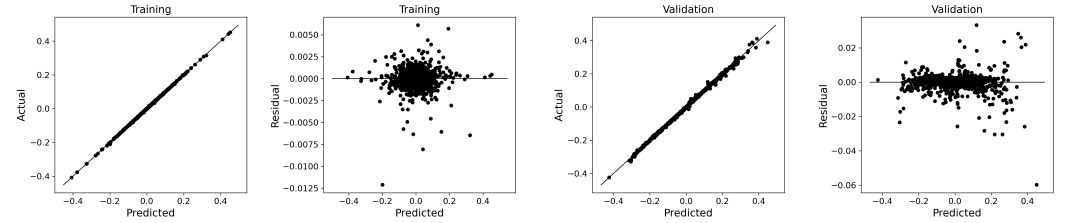

(c) $\Delta\Omega$

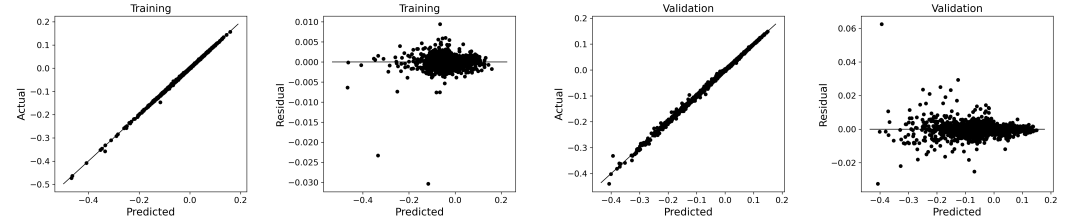

(d) $\Delta\omega$

Fig. 7 Actual and residual by predicted for training and validation for 6400 case design

Table 8 Goodness of fit metrics for training with 6400 case design

	Δe		$\Delta Incl$		$\Delta\Omega$		$\Delta\omega$	
	Training	Validation	Training	Validation	Training	Validation	Training	Validation
R^2	0.9994	0.9991	0.9947	0.9912	0.9998	0.9988	0.9994	0.9987
$RMSE$	0.0002260	0.0002725	0.0006223	0.0008606	0.0005977	0.001401	0.001012	0.001478

The final LHC design considered used 12800 cases, of which 9817, or 76.70%, were physically realisable orbits. Table 9 shows the neural network architectures for each of the outputs. Figure 8 shows the goodness of fit plots and Table 10 shows the R^2 and $RMSE$ values for the training and validation data sets. The goodness of fit metrics and plots indicate much better predictions even for data not used in the training. Better prediction models can be generated using more data.

Table 9 Neural network architectures for 12800 case design

Output	First Layer			Second Layer		
	TanH	Linear	Gaussian	TanH	Linear	Gaussian
Δe	6	6	6	6	6	6
$\Delta Incl$	9	9	9	10	10	10
$\Delta\Omega$	6	6	6	6	6	6
$\Delta\omega$	6	6	6	6	6	6

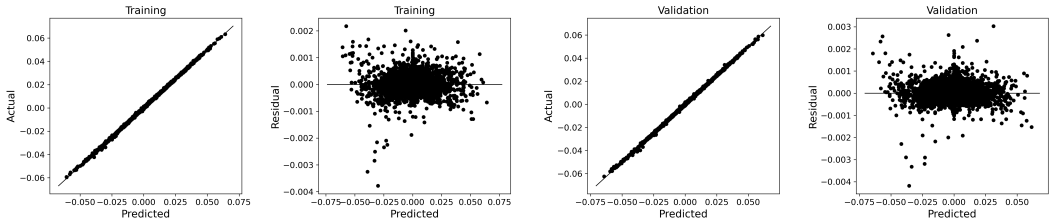

(a) Δe

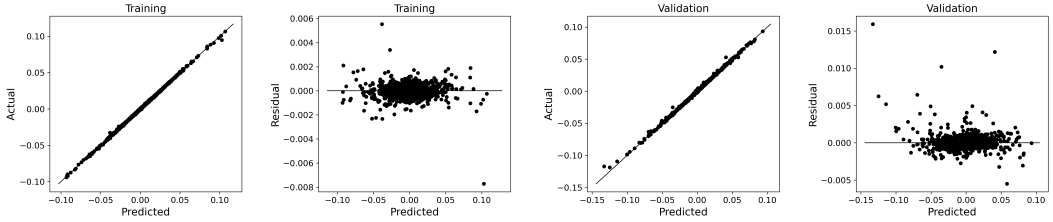

(b) $\Delta Incl$

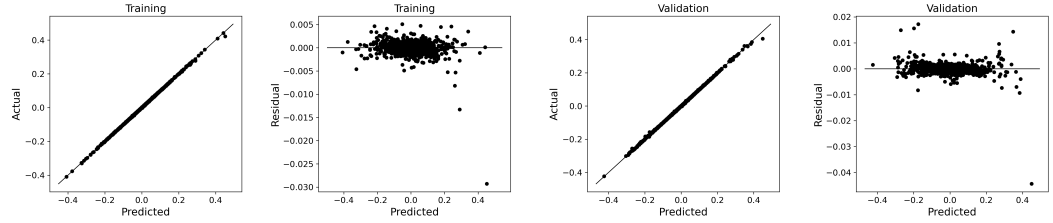

(c) $\Delta\Omega$

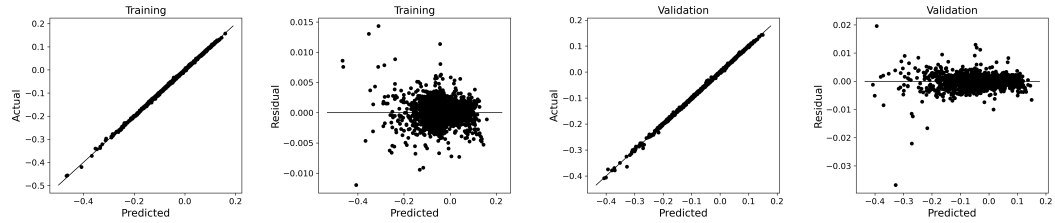

(d) $\Delta\omega$

Fig. 8 Actual and residual by predicted for training and validation for 12800 **case design**

Table 10 Goodness of fit metrics for training with 12800 **case design**

	Δe		$\Delta Incl$		$\Delta\Omega$		$\Delta\omega$	
	Training	Validation	Training	Validation	Training	Validation	Training	Validation
R^2	0.9992	0.9991	0.9994	0.9983	0.9998	0.9996	0.9995	0.9993
$RMSE$	0.0002612	0.0002736	0.0002228	0.0003762	0.0005782	0.0007905	0.0009568	0.001115

D. Capturing Frozen Orbits

It is possible to solve the equations of motion (Equation 1) and set the long period rates of change for eccentricity ($\dot{\bar{e}}$), inclination ($\dot{\bar{i}}$), and argument of perigee ($\dot{\bar{\omega}}$) to 0, thereby achieving a frozen orbit [3]. The orbital parameters that correspond to frozen orbits can then be calculated and plotted, as done in [3]. A similar analysis can be done here, with

the additional inclusion of non-frozen orbits. This is a great advantage to designers who may want to include such orbits in their analysis, incurring the cost of increased station-keeping requirements or limited orbital lifetime, but potentially achieving better mission performance.

A monte carlo analysis was performed to consider a wide range of available orbits. Each of these orbits was analysed using the surrogate models trained using the 12800. A single orbit instability metric IM was calculated by summing the absolute values of the relevant orbital element rates for each case $IM = |\Delta e| + |\Delta di| + |\Delta\omega|$. The absolute values are used because any change is undesirable. A scatter plot of the orbital parameters with the points colored by the instability metric calculated shows areas of the design space with lower orbital instability. As in [3], three different cases are considered: $e = 0$, $\omega = 0, 180$, $\omega = 90, 270$. In this analysis, $\omega = 0$ and $\omega = 270$ are omitted. More details about each of these cases are given in [3].

Figures 9-11 below show the heat maps of the different cases considered. The patterns match those presented in [3]. However, additional information is shown here by considering orbits that are not frozen. The sections of the graph in blue represent orbital parameters that result in low IM value, where red represents high IM value. The points are colored based on the $log(IM)$. Orbits chosen closer to the red sections of the plot would experience higher orbital perturbations. This serves to both validate the approach implemented in this effort by showing that frozen orbits are accurately capture by the surrogate models as well as demonstrate the utility of the surrogate models by considering all possible orbits, not just frozen orbits.

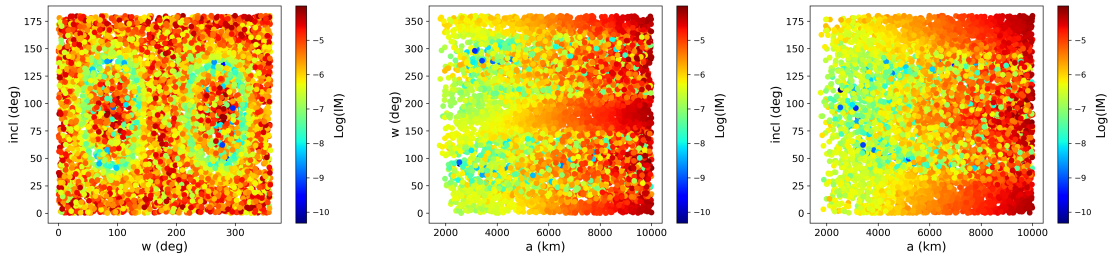

Fig. 9 Heat map for instability metric for cases when $e = 0$

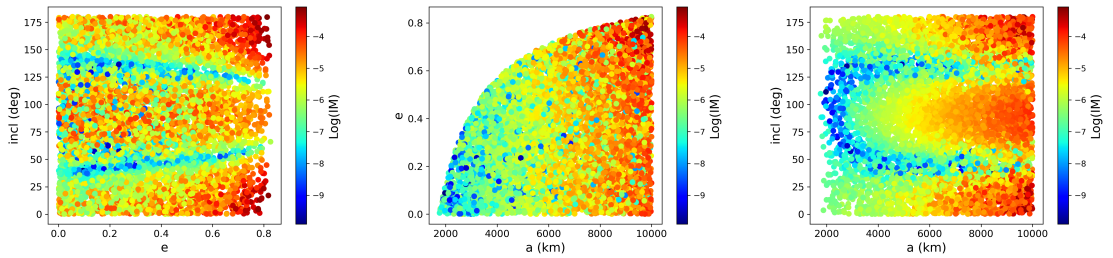

Fig. 10 Heat map for instability metric for cases when $\omega = 90$

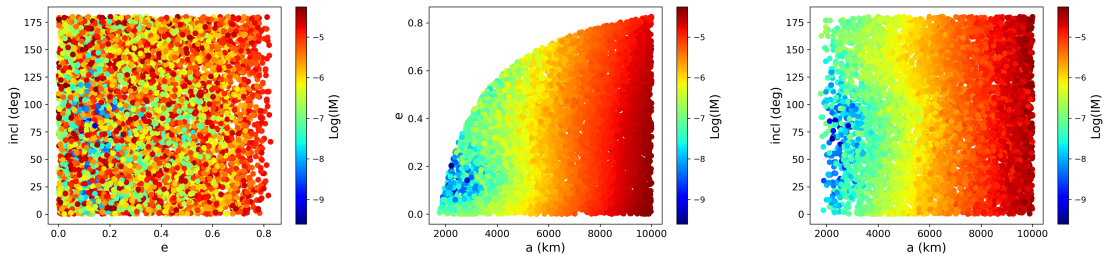

Fig. 11 Heat map for instability metric for cases when $\omega = 180$

The heat maps shown can be considered for any value of the orbital elements. For example, orbits where $i = 90$ deg are not necessarily frozen orbits, but the surrogate models developed can give insight into their stability. Figure 12 shows the results for $i = 90$ deg. There are some frozen orbits in this space, as there do exist frozen orbits when $i = 90$ and $e = 0$ or $\omega = 90, 180$. It is worth mentioning that the results shown in this section are based on a specific formulation of the instability measure IM. Other formulations, such as the product of the errors, may lead to different insights into the data.

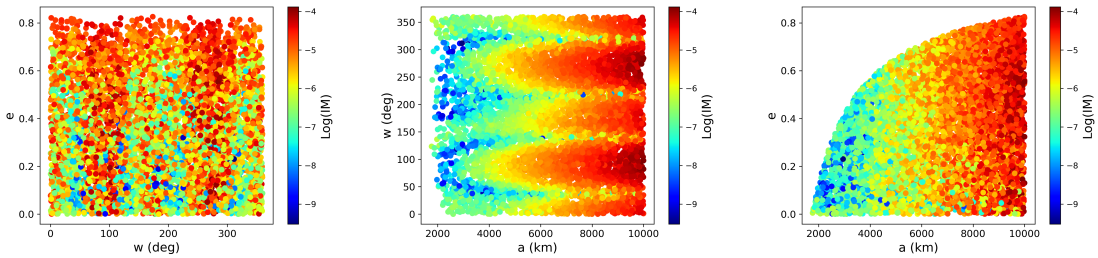

Fig. 12 Heat map for instability metric for cases when $incl = 90$ deg

E. Application to Constellation Design

The goal of this paper was to develop a method to understand the instability of lunar orbits in the context of satellite mission planning or constellation design. As such, a simple example is shown here. Consider an example constellation of 20 satellites with orbital parameters shown in Table 11. In this example, a, e, i, and ω are the same for all the orbits, and Ω is varied to result in 5 different orbital planes. In each orbital plane, the satellites are equally spaced throughout the orbit. From the perspective of the equations of motion in Equation 1, this would mean starting at different values of mean anomaly M, equally spaced between 0 and 2π. While ΔM is not one of the outputs of this model, it is not a variable in the the equations of motion, and therefore the initial value will not change the results of this model as long as an entire orbit is considered.

Table 11 Example satellite constellation

Eccentricity	0
Semi-major axis	4000 km
Argument of Perigee	0
Inclination	45°
# of Orbital Planes	5
# of Sats per Plane	4

For each satellite, the orbital parameters can be input: $e = 0$, $a = 4000km$, $incl = 45$ deg, $\omega = 0$. Ω varies, but like M, it is not a variable in the equations of motion, so it does not need to be directly considered here. In this case, the changes in orbital parameters will be equivalent for all the satellites. The changes are shown in Table 12. If this constellation were to be deployed, these perturbations would need to be accounted for throughout the lifetime of each satellite (assuming the satellite remained in the specified orbit).

VI. Conclusion and Future Work

Increased interest and planned activity in and around the Moon motivates the need for reliable and effective methods to understand the challenges of operating in cislunar space. Lunar orbits, for example, are generally unstable. Many proposed mission plans rely on using frozen orbits, which are stable for longer periods of time. However, this approach drastically limits the available orbits. The goal of this effort was to develop a method to quickly quantify the instability associated with a given lunar orbit. A DoE was conducted to explore the lunar orbital space, and those orbits were propagated using the equations of motion developed for studying frozen orbits. The data was then used to fit surrogate

Table 12 Changes in orbital elements for orbits in example constellation

Orbital Element	ΔValue	Unit
a	0	km
e	8.098×10^{-5}	/
i	0.0001095	rad
Ω	-9.988×10^{-5}	rad
ω	−0.001398	rad
M	6.28	rad

models that accurately predict the changes in orbital parameters during a given orbit. This tool allows designers to quickly quantify instability associated with any orbit within the design ranges considered, shown in Table 1. Higher accuracy surrogate models can be developed using larger data sets. Different ways of using the surrogate models in the context of design were illustrated in Sections V.D and V.E. Additionally, the tool could be integrated into an optimization process or decision making approach with other methods to trade orbit cost with orbit performance. It should be noted that while surrogate models do provide accurate estimates and are extremely useful in design studies where many candidate designs are being considered, any final design selections should be confirmed using the higher fidelity models (in this case the integrated equations of motion).

Several areas of future work would increase the utility of the method and resulting tool presented in this paper. The first would be to continue to refine the surrogate models by generating more data and fitting better neural networks. Another improvement would be to expand the equations of motion to consider more perturbations, including higher order terms in the lunar gravity model and the influence of the sun. The approach would remain the same, but the orbital propagation would necessarily be more complex and time-consuming. Additionally, more complex orbits could be considered, such as orbits around the Lagrange points or around the Earth and the Moon. Such orbits are not well characterized by the classical orbital elements, and the approach presented here would need to be updated to account for the additional complexity. A final avenue for future work mentioned here is to tie the changes in orbital parameters presented here directly to ΔV or fuel requirements for the satellites. Ultimately, the most likely approach for operating in these orbits would be to provide routine station-keeping maneuvers. The real cost would be in the weight of fuel required to maintain the orbit throughout the desired lifetime. An approach to calculate fuel required from the changes in orbital parameters would allow designers to directly consider fuel weight costs associated with any orbits considered.

References

[1] William Gerstenmaier, J. C., "Cislunar and Gateway Overview," , Accessed 05/30/2022. URL https://www.nasa.gov/sites/default/files/atoms/files/cislunar-update-gerstenmaier-crusan-v5a_tagged_0.pdf.

[2] Thomas J. Colvin, R. L. B. L., Keith W. Crane, "Demand Drivers of the Lunar and Cislunar Economy," *Science and Technology Policy Institute*, 2020.

[3] Nie, T., and Gurfil, P., "Lunar frozen orbits revisited," *Celestial Mechanics and Dynamical Astronomy*, Vol. 130, No. 10, 2018. https://doi.org/10.1007/s10569-018-9858-0.

[4] Singh, S. K., Woollands, R., Taheri, E., and Junkins, J., "Feasibility of quasi-frozen, near-polar and extremely low-altitude lunar orbits," *Acta Astronautica*, Vol. 166, 2020, p. 450–468. https://doi.org/10.1016/j.actaastro.2019.10.037.

[5] NASA, "NASA - Artemis Mission," , Accessed: 05 2022. URL https://www.nasa.gov/specials/artemis/.

[6] Clark, S., "NASA's Lunar Gateway: The plans for a permanent space station that will orbit the Moon," , 02 2022. URL https://www.sciencefocus.com/space/nasa-lunar-gateway/.

[7] Israel, D. J., Mauldin, K. D., Roberts, C. J., Mitchell, J. W., Pulkkinen, A. A., Cooper, L. V., Johnson, M. A., Christe, S. D., and Gramling, C. J., "LunaNet: A flexible and Extensible Lunar Exploration Communications and Navigation Infrastructure," *2020 IEEE Aerospace Conference*, 2020. https://doi.org/10.1109/aero47225.2020.9172509.

[8] Mazarico, E., "Lunar Gravity Field: GRGM1200A," , Accessed: 05 2022. URL https://pgda.gsfc.nasa.gov/products/50.

[9] Bhamidipati, S., Mina, T., and Gao, G., "A case study analysis for designing a lunar navigation satellite system with time-transfer from Earth-GPS," *The International Technical Meeting of the The Institute of Navigation*, 2022. https://doi.org/10.33012/2022.18202.

[10] "NASA - Moon," , Accessed 12/04/2022. URL https://www.grc.nasa.gov/www/k-12/rocket/moon.html.

[11] JPL, "NASA's GRAIL Mission Solves Mystery of Moon's Surface Gravity," , Accessed: 05 2022. URL https://www.jpl.nasa.gov/news/nasas-grail-mission-solves-mystery-of-moons-surface-gravity.

[12] Prussing, J. E., and Conway, B. A., *Orbital Mechanics*, Oxford University Press, 2013.

[13] Nie, T., Gurfil, P., and Zhang, S., "Bounded lunar relative orbits," *Acta Astronautica*, Vol. 157, 2019, pp. 500–516.

[14] Giacaglia, G. E., Murphy, J. P., and Felsentreger, T. L., "A semi-analytic theory for the motion of a lunar satellite," *Celestial Mechanics*, Vol. 3, No. 1, 1970, p. 3–66. https://doi.org/10.1007/bf01230432.

[15] "Latin Hypercube Design," , 11/10/2021. URL https://www.jmp.com/support/help/en/16.2/index.shtml#page/jmp/visualizing-the-latin-hypercube-design.shtml#.

[16] Qian, P. Z., "Nested Latin hypercube designs," *Biometrika*, Vol. 96, No. 4, 2009, pp. 957–970.

[17] Krose, B., and Smagt, P. v. d., *An introduction to neural networks*, 2011.

[18] Dubey, S. R., Singh, S. K., and Chaudhuri, B. B., "Activation functions in deep learning: A comprehensive survey and benchmark," *Neurocomputing*, 2022.

[19] Sall, J., Stephens, M. L., Lehman, A., and Loring, S., *JMP start statistics: a guide to statistics and data analysis using JMP*, Sas Institute, 2017.

[20] Yadav, S., and Shukla, S., "Analysis of k-fold cross-validation over hold-out validation on colossal datasets for quality classification," *2016 IEEE 6th International conference on advanced computing (IACC)*, IEEE, 2016, pp. 78–83.